Automated real-time formation evaluation from cuttings and drilling data analysis: State of the art

Harpreet Singh, Chengxi Li, Peng Cheng, Xunjie Wang, Ge Hao, Qing Liu

China National Petroleum Corporation USA, Houston, Texas 7704

1 Appendix

1.1 Densities and Porosities from NMR

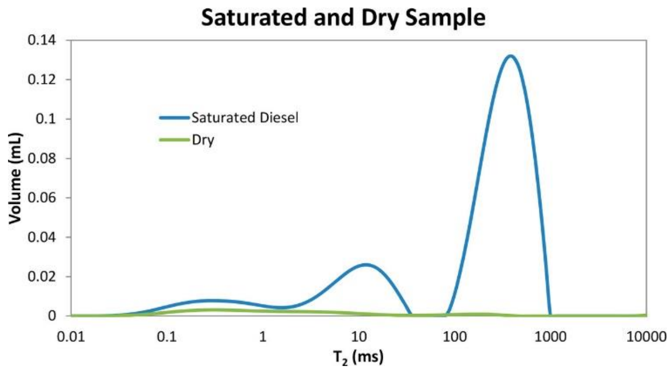

Figure A- 1: T2 relaxation times for cutting samples saturated with diesel (blue legend) and after drying (green legend). From (Althaus et al., 2020).

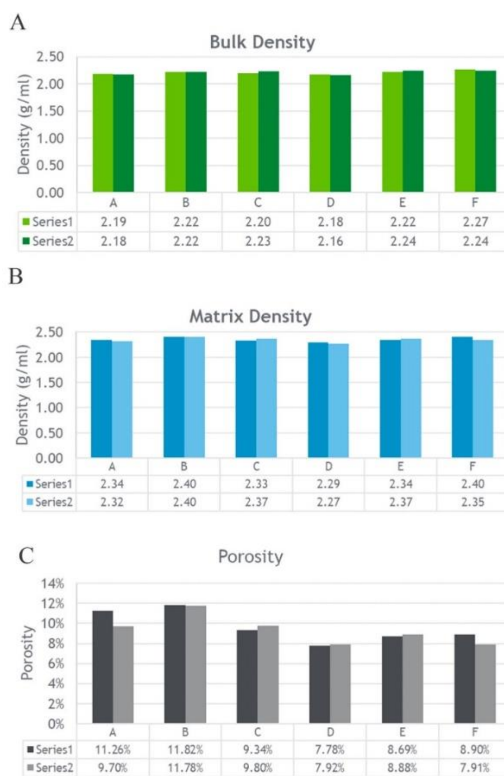

Bulk Density	A	B	C	D	E	F
Series1	2.19	2.22	2.20	2.18	2.22	2.27
Series2	2.18	2.22	2.23	2.16	2.24	2.24

Matrix Density	A	B	C	D	E	F
Series1	2.34	2.40	2.33	2.29	2.34	2.40
Series2	2.32	2.40	2.37	2.27	2.37	2.35

Porosity	A	B	C	D	E	F
Series1	11.26%	11.82%	9.34%	7.78%	8.69%	8.90%
Series2	9.70%	11.78%	9.80%	7.92%	8.88%	7.91%

Figure A- 2: NMR-based measured values of bulk density, matrix density, and porosity, for two batches of samples (series 1 and series 2, respectively, separated prior to cleaning) to ensure repeatability. From (Althaus et al., 2020).

1.2 Permeability Prediction

1.2.1 Numerical Model

The model is derived using perfect gas law (Eqn. A- 1), mass balance (Eqn. A- 2), momentum balance (Darcy's law; Eqn. A- 3)

$$S_g = S_{g0}\frac{P_0}{P} \qquad \text{Eqn. A- 1}$$

$$\operatorname{div}(\overrightarrow{V_0}) + \phi\frac{\partial S_0}{\partial t} = 0 \qquad \text{Eqn. A- 2}$$

$$\overrightarrow{V_0} = -\frac{K}{\mu_0}\nabla(P_{oil}) \qquad \text{Eqn. A- 3}$$

Using Eqn. A- 1:

$$\frac{\partial S_0}{\partial t} = \frac{\partial S_0}{\partial P}\frac{\partial P}{\partial t} = \left(S_{g0}\frac{P_0}{P^2}\right)\frac{\partial P}{\partial t} \qquad \text{Eqn. A- 4}$$

Substituting Eqn. A- 3 and Eqn. A- 4 in Eqn. A- 2:

$$\Delta P = \frac{\mu_0 \phi S_{g0}}{K}\frac{P_0}{P^2}\frac{\partial P}{\partial t} \qquad \text{Eqn. A- 5}$$

Writing Eqn. A- 5 in spherical coordinates, which gives the pressure diffusion equation (Eqn. A- 6) weighted by initial gas saturation (S_{g0}) and a factor $1/P^2$ (due to compressibility) as follows:

$$\frac{\partial}{\partial r}\left(r^2\frac{\partial P}{\partial r}\right) = \alpha\frac{r^2}{P^2}\frac{\partial P}{\partial t} \qquad \text{Eqn. A- 6}$$

Where, $\alpha = \frac{\mu_0 \phi S_{g0} P_0}{K}$

Using the variables given in Eqn. A- 7 and Eqn. A- 8 (coefficient of diffusion), Eqn. A- 6 is converted to a dimensionless form given by Eqn. A- 9.

$$P^* = \frac{P}{P_0}, \quad r^* = \frac{r}{r_{max}}, \quad t^* = \frac{tD}{r_{max}^2} \qquad \text{Eqn. A- 7}$$

$$D = \frac{KP_0}{\phi S_{g0}\mu} \qquad \text{Eqn. A- 8}$$

$$\frac{1}{r^{*2}}\frac{\partial}{\partial r^*}\left(r^{*2}\frac{\partial P^*}{\partial r^*}\right) = \frac{1}{P^{*2}}\frac{\partial P^*}{\partial t^*} \qquad \text{Eqn. A- 9}$$

Permeability is obtained through an inverse solution of Eqn. A- 9, which is solved in two stages that represent the two boundary conditions, respectively, which are i) a period of constant injection rate, and ii) a period of constant injection pressure. The boundary and initial conditions used in solving the model are as follows:

Boundary conditions:

$$\frac{\partial P}{\partial r}(0,t) = 0 \quad \text{Eqn. A- 10}$$

$$P(1,t) = P_{ext} \quad \text{Eqn. A- 11}$$

Initial condition:

$$P(r,0) = 1 \quad \text{Eqn. A- 12}$$

The first boundary condition (Eqn. A- 10) is used to deduce P_{ext} through a loop of convergence as described by a flowchart in Figure A- 3(a), where Eqn. A- 9 is solved in an explicit finite difference scheme. The P_{ext} at the end of the initial period (first boundary condition) is now used to calculate the pressure profile using the pressure diffusion equation (Eqn. A- 6) and the corresponding volume of oil injected during the second stage of the experiment from the gas saturation profile.

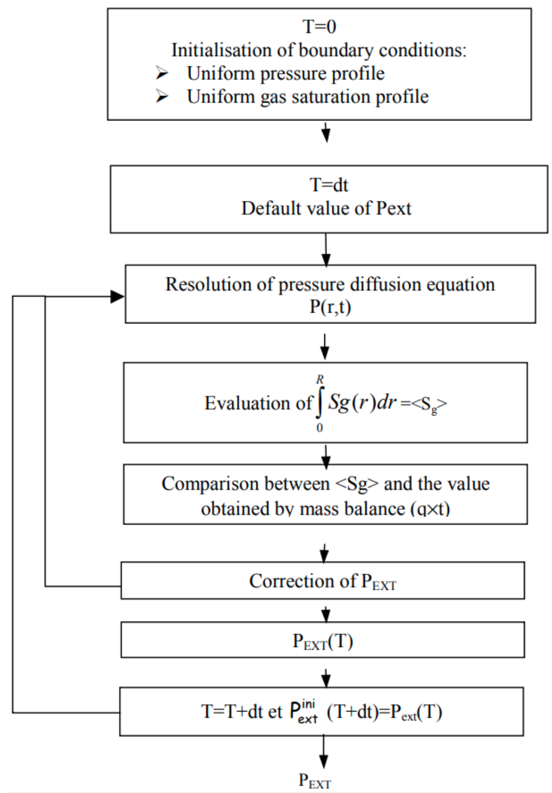

(a)

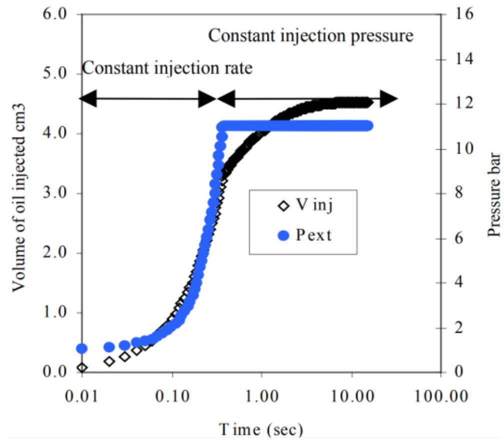

(b)

Figure A- 3: (a) Steps to calculate P_{ext} using a convergence criterion. (b) An example depicting the solution from the model that involves two-stages depicting two different boundary conditions. From (Egermann et al., 2002).

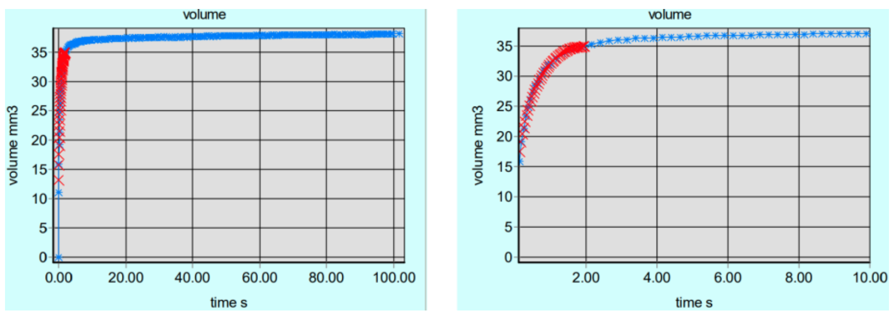

(a)

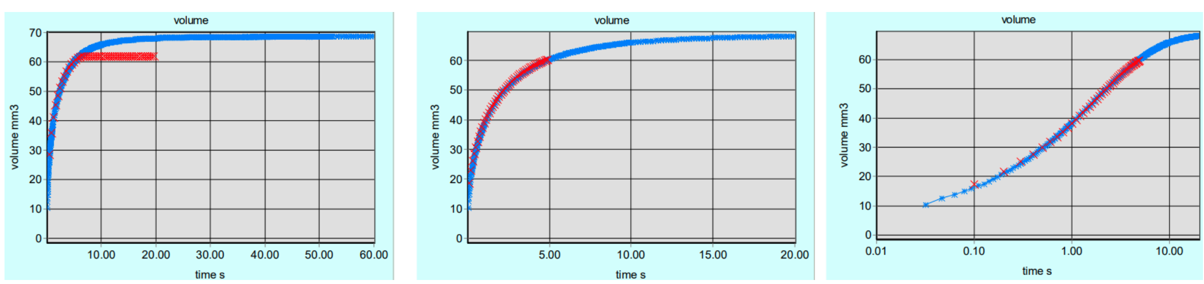

(b)

Figure A- 4: Total volume of oil injected into the cuttings with time for (a) chalk sample with a porosity of 0.35, (b) carbonate sample with a porosity of 0.23. (Lenormand and Fonta, 2007)

1.3 Machine Learning-Based Classification of Rock Types

1.3.1 Application-1

Figure A- 5: Illustration of the workflow of the deep learning approach to identify intra-class and inter-class rock types, including variation in shale and colors, from the same image of the drill cuttings (Tamaazousti et al., 2020).

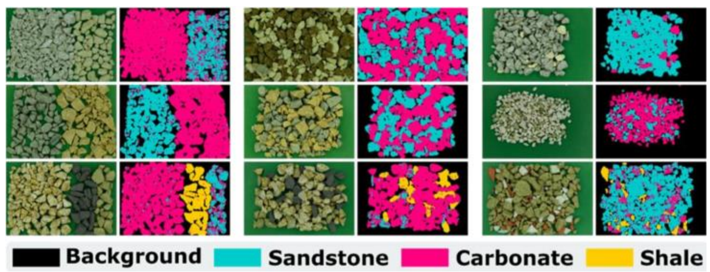

Figure A- 6: Results of the trained model when applied on blind images of cuttings that contained mixture of lithologies, where the top two rows contain cuttings from sandstone and carbonate lithologies, whereas the last row contains all the three lithologies (sandstone, carbonate, and shale). From (Tamaazousti et al., 2020).

1.3.2 Application-2

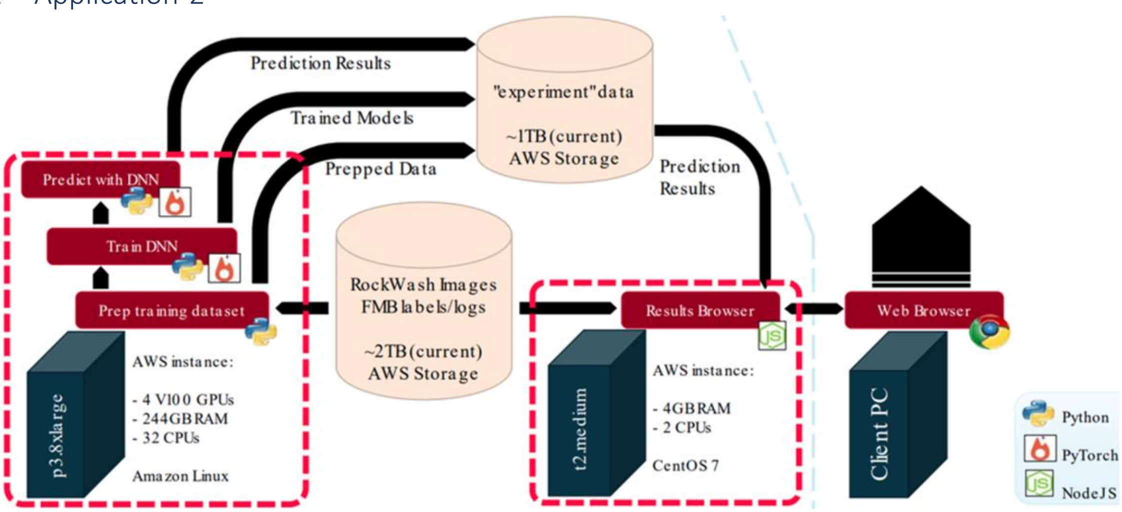

(a)

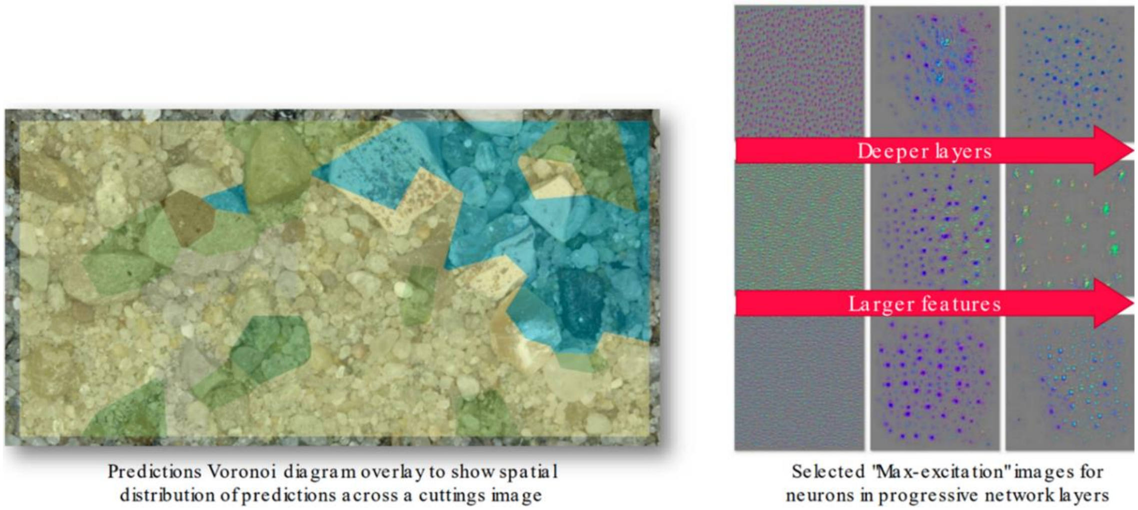

(b)

Figure A- 7: (a) Architecture of Equinor's cuttings image lithology interpretation with neural-networks (Cuillin) tool. From (Equinor, 2019). (b) Visualizations of the multi-class lithology classification and DNN predictions in Cuillin. From (Equinor, 2019).

1.3.3 Application-3

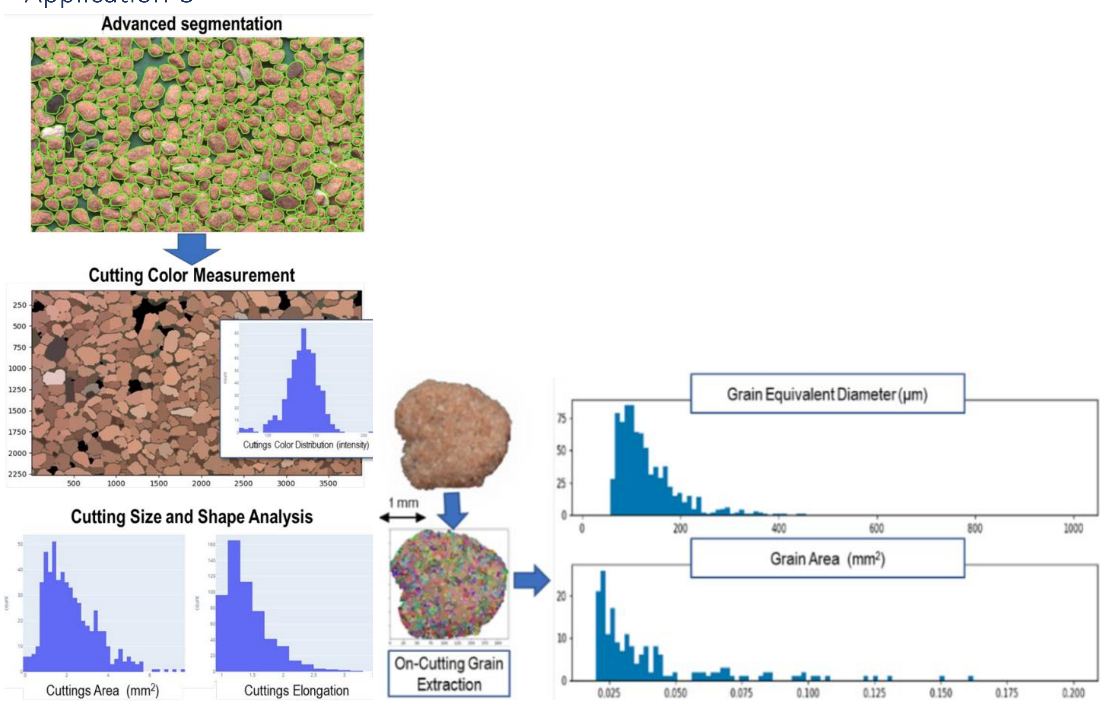

(a)

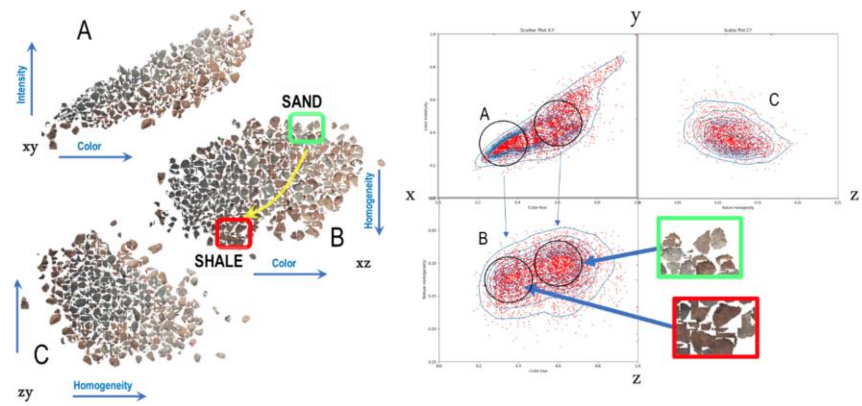

(b)

Figure A- 8: (a) Object based image analysis used to identify color, shape, and size for characterization and analysis of the particles, including the characterization of cuttings with grainy texture. From (Di Santo et al., 2022). (b) Particle clustering differentiating sand from shale based on color intensity, color hue and texture homogeneity. From (Di Santo et al., 2022).

1.4 DRIFTS Model

Table A- 1: Mechanical properties of the standard mineral components and brine as used in the DRIFTS measurements. From (Prioul et al., 2018).

Mineral and fluid components	**Density (kg/m3)**	**Bulk modulus (GPa)**	**Shear modulus (GPa)**	**P-wave modulus (GPa)**	**Reference**
Clay (cla)	2.80	22.1	8.5	33.4	(Vernik and Kachanov, 2010)
Quartz + Feldspar + Mica (qfm)	2.65	36.6	45.0	96.6	(Ellis et al., 1988)
Calcite	2.71	76.8	32.0	119.5	(Ellis et al., 1988)
Dolomite	2.87	76.4	49.7	142.7	(Mavko et al., 2009)
Pyrite	5.01	138.6	109.8	285.0	(Ellis et al., 1988)
TOM*	1.10	3.4	2.7	7.0	(Prioul et al., 2018)
Brine	1.06	2.2	–	2.2	(Mavko et al., 2009)

**The values for the organic matter are a function of the maturity and are given solely as an example of values for the studied case (the effective organic matter values given here also include kerogen, hydrocarbon, and bitumen, and so they are not pure kerogen values).*

1.4.1 Elasticity Conventions for Anisotropic Medium

A TI medium (e.g., organic-rich shales) are classified with 5 independent elastic stiffness constants ($C_{11}, C_{33}, C_{55}, C_{66}, C_{13}$) that are related to elastic engineering constants as discussed below.

$$C_{ij} = \begin{pmatrix} C_{11} & C_{12} & C_{13} & 0 & 0 & 0 \\ C_{12} & C_{11} & C_{13} & 0 & 0 & 0 \\ C_{13} & C_{13} & C_{33} & 0 & 0 & 0 \\ 0 & 0 & 0 & C_{55} & 0 & 0 \\ 0 & 0 & 0 & 0 & C_{55} & 0 \\ 0 & 0 & 0 & 0 & 0 & C_{66} \end{pmatrix} \quad \text{Eqn. A- 13}$$

$$S_{ij} = C_{ij}^{-1} = \begin{pmatrix} \frac{1}{E_H} & -\frac{\nu_H}{E_H} & -\frac{\nu_V}{E_V} & 0 & 0 & 0 \\ -\frac{\nu_H}{E_H} & \frac{1}{E_H} & -\frac{\nu_V}{E_V} & 0 & 0 & 0 \\ -\frac{\nu_V}{E_V} & -\frac{\nu_V}{E_V} & \frac{1}{E_V} & 0 & 0 & 0 \\ 0 & 0 & 0 & \frac{1}{G_V} & 0 & 0 \\ 0 & 0 & 0 & 0 & \frac{1}{G_V} & 0 \\ 0 & 0 & 0 & 0 & 0 & \frac{1}{G_V} \end{pmatrix} \qquad \text{Eqn. A- 14}$$

Where,

$$C_{11} = \frac{E_H\left(1 - \frac{E_H}{E_V}\nu_V^2\right)}{D} \qquad \text{Eqn. A- 15}$$

$$C_{33} = \frac{E_V(1 - \nu_H^2)}{D} \qquad \text{Eqn. A- 16}$$

$$C_{12} = \frac{E_H\left(\frac{E_H}{E_V}\nu_V^2 + \nu_H\right)}{D} \qquad \text{Eqn. A- 17}$$

$$C_{13} = \frac{E_H\nu_V(\nu_H + 1)}{D} \qquad \text{Eqn. A- 18}$$

$$C_{55} = G_V \qquad \text{Eqn. A- 19}$$

$$C_{66} = G_H \qquad \text{Eqn. A- 20}$$

$$D = (1 + \nu_H)\left(1 - 2\frac{E_H}{E_V}\nu_V^2 - \nu_H\right) \qquad \text{Eqn. A- 21}$$

Conversely, the elastic parameters (E_V, E_H, ν_V, ν_H) and anisotropy parameters ($\varepsilon, \delta, \gamma$) can be expressed as a function of the elastic stiffness constants as follows:

$$E_V = C_{33} - 2\left(\frac{C_{13}^2}{C_{11} + C_{12}}\right) \qquad \text{Eqn. A- 22}$$

$$E_H = \frac{(C_{11} - C_{12})(C_{11}C_{33} - 2C_{13}^2 + C_{12}C_{33})}{C_{33}C_{11} - C_{13}^2} \qquad \text{Eqn. A- 23}$$

$$\nu_V = \frac{C_{13}}{C_{11} + C_{12}} \qquad \text{Eqn. A- 24}$$

$$\nu_H = \frac{C_{33}C_{12} - C_{13}^2}{C_{33}C_{11} - C_{13}^2}$$ Eqn. A- 25

$$\varepsilon = \frac{C_{11} - C_{33}}{2C_{33}}$$ Eqn. A- 26

$$\delta = \frac{(C_{13} + C_{55})^2 - (C_{33} - C_{55})^2}{2C_{33}(C_{33} - C_{55})}$$ Eqn. A- 27

$$\gamma = \frac{C_{66} - C_{55}}{2C_{55}}$$ Eqn. A- 28

1.4.2 Rock-Physics Model

$$C_{33}^{mtom} = \left[\frac{\varphi_{tom}}{M_{tom}} + \sum_i \frac{\varphi_{m,i}}{M_i}\right]^{-1}$$ Eqn. A- 29

$$C_{55}^{mtom} = \left[\frac{\varphi_{tom}}{G_{tom}} + \sum_i \frac{\varphi_{m,i}}{G_i}\right]^{-1}$$ Eqn. A- 30

$$C_{66}^{mtom} = \theta\left[\varphi_{tom}G_{tom} + \sum_i \varphi_{m,i}G_i\right] + (1-\theta)\left[\frac{\varphi_{tom}}{G_{tom}} + \sum_i \frac{\varphi_{m,i}}{G_i}\right]^{-1}$$ Eqn. A- 31

$$C_{33} = C_{33}^{mtom} g_\phi(\varphi_w) + h_{fl}(\varphi_w, M_w)$$ Eqn. A- 32

$$C_{55} = C_{55}^{mtom} g_\phi(\varphi_w)$$ Eqn. A- 33

$$C_{66} = C_{66}^{mtom} g_\phi(\varphi_w)$$ Eqn. A- 34

$$\gamma = \frac{\theta}{2}\frac{\left(\left[\varphi_{tom}G_{tom} + \sum_i \varphi_{m,i}G_i\right] - \left[\frac{\varphi_{tom}}{G_{tom}} + \sum_i \frac{\varphi_{m,i}}{G_i}\right]^{-1}\right)}{\left[\frac{\varphi_{tom}}{G_{tom}} + \sum_i \frac{\varphi_{m,i}}{G_i}\right]^{-1}}$$ Eqn. A- 35

1.4.3 Dynamic Elasticity Model from Laboratory Measurements on Core Samples

Ultrasonic P- and S-wave velocities measurement using 3 core plugs (1 cut parallel to, 1 perpendicular to, and 1 at 45° to the symmetry axis) to derive five independent dynamic elastic constants:

$$\varepsilon^{dyn} = a_1\gamma^{dyn}$$ Eqn. A- 36

$$\frac{C_{13}^{dyn}}{C_{12}^{dyn}} = 1 - a_2\varepsilon^{dyn}$$ Eqn. A- 37

1.4.4 Estimation of Unknown Parameters for the Rock-Physics Model

- Unknown parameters: $C_{11}, C_{12}, C_{13}, C_{33}, C_{55}, C_{66}$
- Initially known parameters:
  - $\varphi_{m,i}, \varphi_w, \varphi_{tom}$: volumes known from well-logs (or drill cuttings with DRIFTS measurements).
  - M_i, G_i, M_w: moduli values for mineral components (i), and water known from a chart.
- Trial parameter: θ
- Method of estimating unknown parameters:
  - C_{33}, C_{55}: Using the known parameters and trial values for M_{tom}, G_{tom}, C_{33} is computed using equations for Eqn. A- 29 and Eqn. A- 32, whereas C_{55} using Eqn. A- 30 and Eqn. A- 33. The effective organic matter moduli values (M_{tom}, G_{tom}) in these equations are iterated and the output values of C_{33}, C_{55} are compared against the moduli values derived from sonic-log until a satisfactory match is achieved. At this stage, the moduli values for total organic matter (M_{tom}, G_{tom}) are also known.
  - C_{66}: Using the known parameters, organic matter moduli estimated in previous step (M_{tom}, G_{tom}), and a trial parameter (θ), C_{66} is computed using equations for Eqn. A- 31 and Eqn. A- 34. The trial parameter value is iterated and the output values of C_{66} is compared against the moduli value derived from sonic-log until a satisfactory match is achieved.
  - C_{11}: Using $\varepsilon \left(= \frac{C_{11}-C_{33}}{2C_{33}}\right)$, C_{33} (estimated in first step), γ (from Eqn. A- 35), and Eqn. A- 36, C_{11} can be estimated from $C_{11} = C_{33}(1+2\varepsilon) = C_{33}(1+2a_1\gamma)$.
  - C_{13}: Using C_{11} (estimated in previous step), Eqn. A- 34 to Eqn. A- 36, parameters a_1 and a_2, C_{13} can be estimated from $C_{13} = C_{12}(1-a_2\varepsilon) = (C_{11}-2C_{66})(1-a_2a_1\gamma)$.

1.4.5 Dynamic to Static Elasticity Model

In order to estimate geomechanical properties of the rock, dynamic properties characterized through sonic log and the rock-physics model are transformed to their static equivalent values with the following relationships, where the parameters b_1, b_2, b_3, b_4 are determined through laboratory data.

$$\varepsilon^{sta} = b_1\gamma^{sta} \qquad \text{Eqn. A- 38}$$

Typically, Eqn. A- 36 is also valid for static data, in which case we get $b_1 = a_1$.

$$\frac{C_{13}^{sta}}{C_{12}^{sta}} = 1 - b_2\varepsilon^{sta} \qquad \text{Eqn. A- 39}$$

$$\frac{C_{11}^{sta}}{C_{11}^{dyn}} = \frac{C_{66}^{sta}}{C_{66}^{dyn}} = b_3 \qquad \text{Eqn. A- 40}$$

$$\varepsilon^{sta} = b_4\varepsilon^{dyn} \qquad \text{Eqn. A- 41}$$

Using a system of equations from Eqn. A- 38 to Eqn. A- 41, and 5 dynamic elastic parameters obtained through log- or DRIFTS-based data, all 5 independent static elastic parameters ($C_{11}, C_{13}, C_{33}, C_{55}, C_{66}$) can be estimated.

1.4.6 Minimum Horizontal Stress (Geomechanical Model)

$$\boxed{\sigma_h = \frac{E_H}{E_V}\frac{\nu_V}{(1-\nu_H)}(\sigma_V - \alpha_V P_P) + \frac{E_H}{(1-\nu_H^2)}(\varepsilon_h + \nu_H \varepsilon_H) + \alpha_H P_P} \quad \text{Eqn. A- 42}$$

$$\boxed{\sigma_h = \frac{C_{13}}{C_{33}}(\sigma_V - \alpha_V P_P) + \left(C_{11} - \frac{C_{13}^2}{C_{33}}\right)\varepsilon_h + \left(C_{12} - \frac{C_{13}^2}{C_{33}}\right)\varepsilon_H + \alpha_H P_P} \quad \text{Eqn. A- 43}$$

Where,

$$\alpha_H = 1 - \left(\frac{C_{11} + C_{12} + C_{13}}{3K_s}\right) \quad \text{Eqn. A- 44}$$

$$\alpha_V = 1 - \left(\frac{2C_{13} + C_{33}}{3K_s}\right) \quad \text{Eqn. A- 45}$$

Therefore, in-situ stress in an unconventional formation can be estimated using cutting-based measurements and Eqn. A- 42 (or Eqn. A- 43), where the input parameters in Eqn. A- 42 (or Eqn. A- 43) can be estimated as discussed in the above workflow.

Table A- 2: Description of parameters used in geomechanics model, and the corresponding method of estimation for each parameter.

Variable	**Description**	**Method of estimation**
$W_{mo,i}$	Weight fractions of the mineral component i on a with-organic matter basis	Measured through DRIFTS.
W_{tom}^{drifts}	Weight fraction of the organic matter on a with-organic matter basis	Measured through DRIFTS.
W_{ker}	Weight fraction of the kerogen on a with-organic matter basis	Measured through DRIFTS. For drill cuttings, this is equal to W_{tom}^{drifts}.
ρ_{mo}^{drifts}	Density of the combined inorganic and organic phases	Measured through DRIFTS.
σ_h	Minimum horizontal stress	Using Eqn. A- 42 or Eqn. A- 43.
σ_H	Maximum horizontal stress	
σ_V	Vertical stress	By depth-integration of the bulk density.
α_H	Horizontal Biot's coefficient	Using Eqn. A- 44
α_V	Vertical Biot's coefficient	Using Eqn. A- 45
P_P	Pore pressure	Using drilling data or direct measurements.
ε_h	Strain in the direction of minimum horizontal stress	Using Eqn. A- 42 or Eqn. A- 43 with input of the elastic constants and point-wise σ_h test measurements.
ε_H	Strain in the direction of maximum horizontal stress	Using Eqn. A- 42 or Eqn. A- 43 with input of the elastic constants and point-wise σ_h test measurements.
K_s	Solid modulus of the grains	Standard value.
C_{11}, C_{66}	Bedding-parallel elastic moduli	As described under section 1.4.4.
C_{33}, C_{55}	Bedding-normal elastic moduli	As described under section 1.4.4.

M_i	Isotropic compressional elastic moduli for mineral component i	Using Table A- 1.
G_i	Isotropic shear elastic moduli for mineral component i	Using Table A- 1.
M_{tom}	Trial value of the isotropic compressional elastic moduli for organic matter	Through trial and iteration.
G_{tom}	Trial value of the isotropic shear elastic moduli for organic matter	Through trial and iteration.
θ	Constant parameter between 0 and 1	As described under section 1.4.4.
$g_\phi(\varphi_w)$	Water porosity multiplier	Using data and fitting it to $(1 - A\varphi_w)$ for low-porosity (<5%) rocks.
$h_{fl}(\varphi_w, M_w)$	Pore space modulus	Using Gassmann fluid substitution expression: $\frac{\alpha^2 M_w}{\varphi_w}$. Here, α is the Biot's coefficient and is calculated from the porosity law.
M_w	Water's compressional modulus	Standard value.
γ	Shear anisotropic parameter	Using Eqn. A- 35.

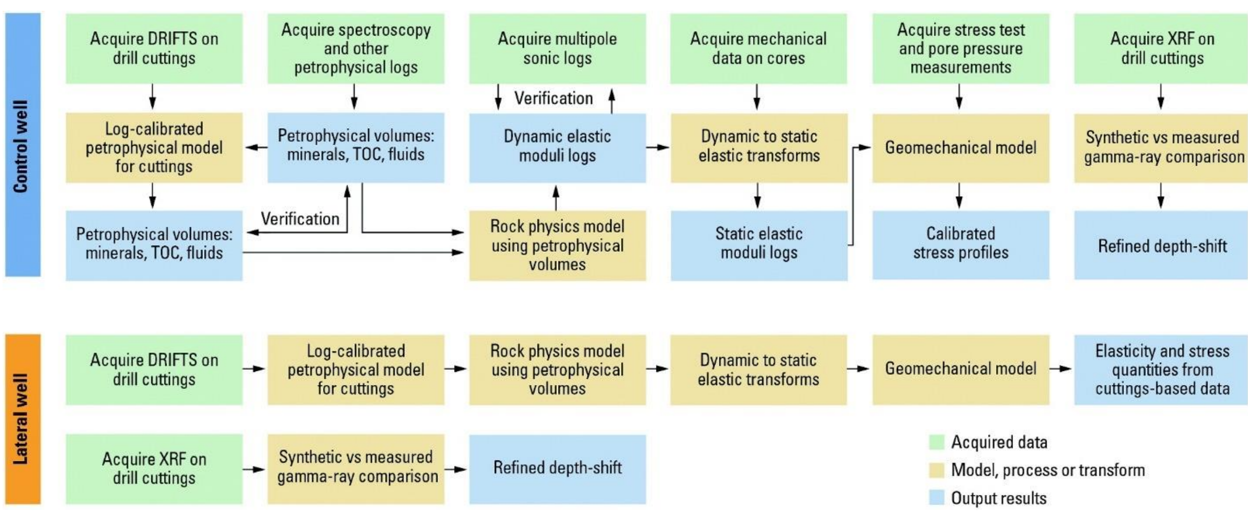

Figure A- 9: Flowchart summarizing the procedure to estimate geomechanical model using the DRIFTS measurements on drill cuttings. From (Prioul et al., 2018).

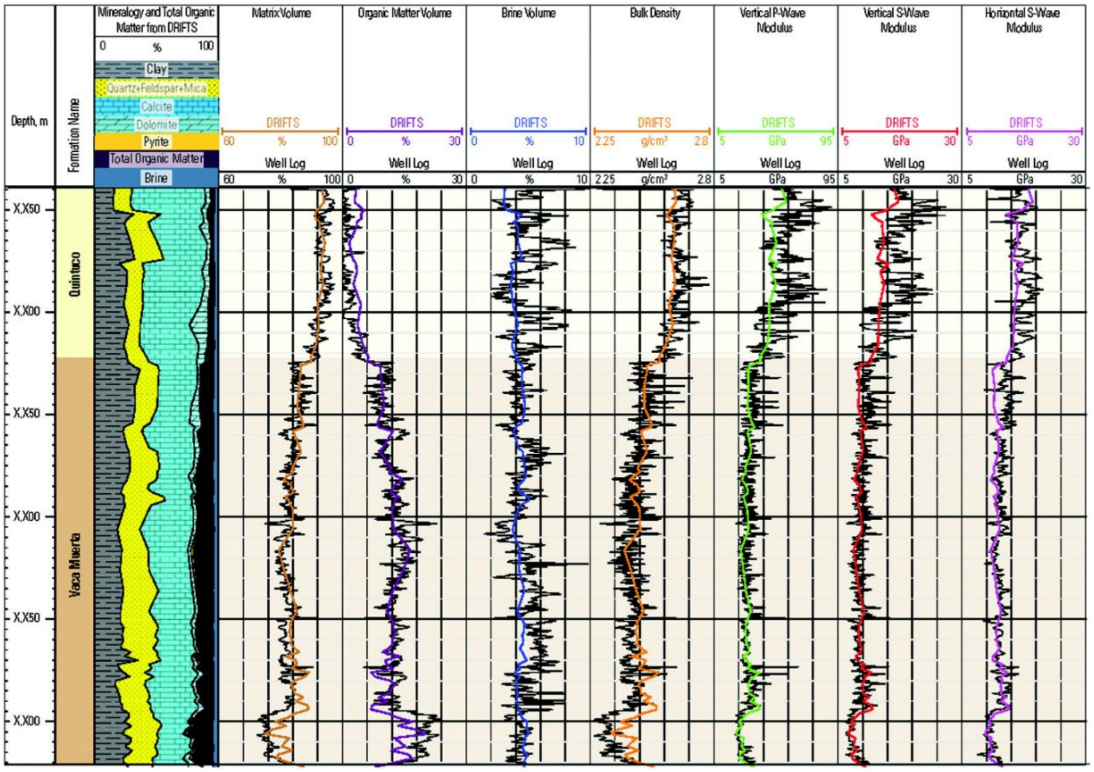

Figure A- 10: Validation of the geomechanical properties estimated using the DRIFTS measurements on drill cuttings with their corresponding well-log measurements. From (Prioul et al., 2018).

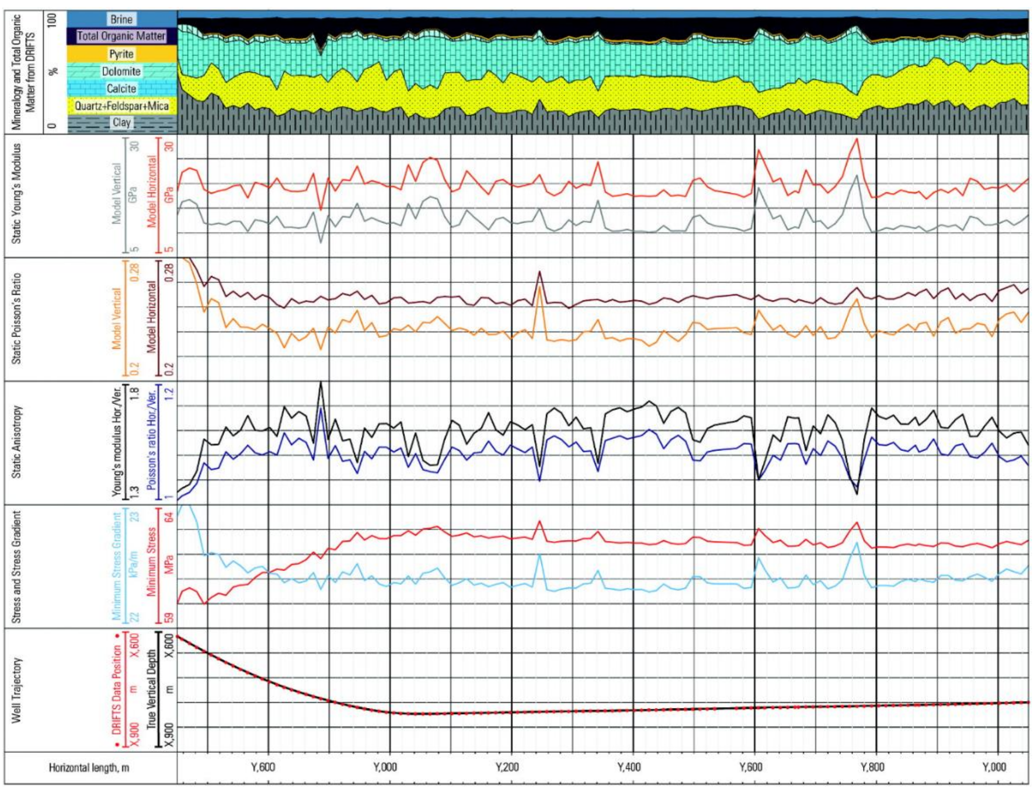

Figure A- 11: Petrophysical volumes, static elastic properties, static anisotropy, and the minimum stress stress gradient estimated using the DRIFTS measurements on drill cuttings from a horizontal lateral in Vaca Muerta formation. From (Prioul et al., 2018).

1.5 Micro/Nano Indentation Method

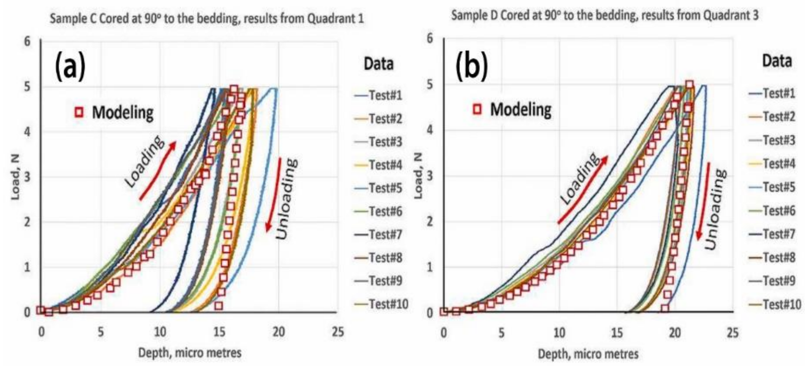

(a)

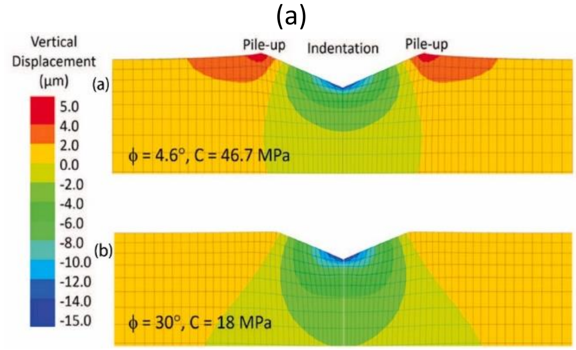

(b)

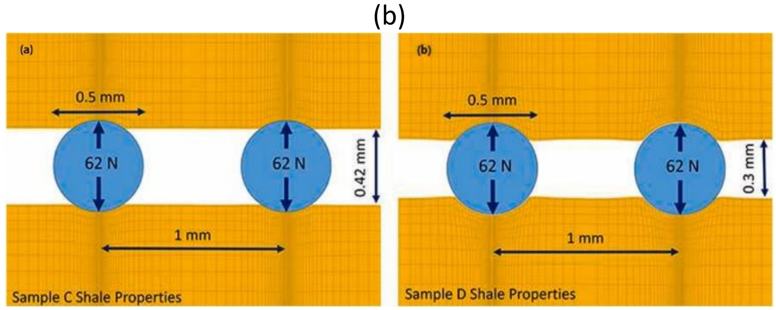

(c)

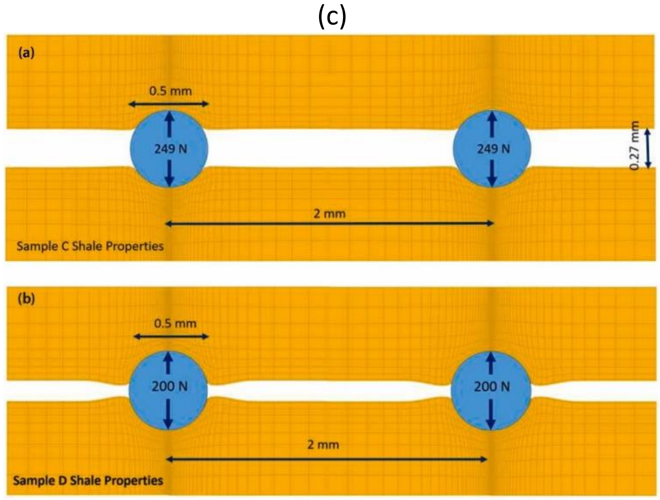

(d)

Figure A- 12: (a) Experimental and modeled indentation curves for the Caney shale samples. (b) 2-D visualization of the modeled indentation pit for two Caney shale samples after unloading. (c)-(d) 2-D visualizations of the modeled proppant embedment (due *to elastic and plastic shale deformations) for two Caney shale samples with varied distance between the proppants. From (Katende et al., 2021).*

1.6 Inclined Direct Shear Testing Device (IDSTD)

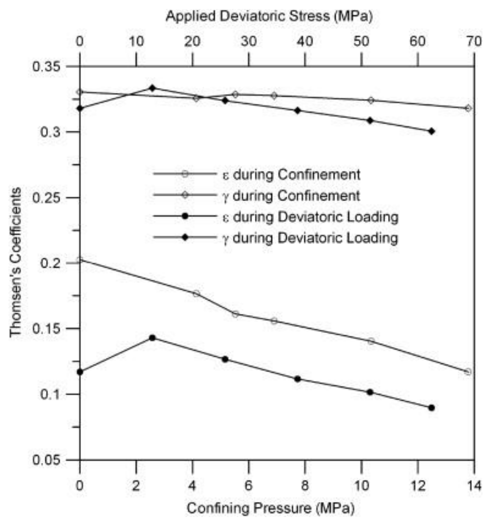

Figure A- 13: Variation in degree of anisotropy (anisotropy ratios of P-wave and S-wave during hydrostatic confinement and deviatoric loading) during confinement (13.79 MPa) and during deviatoric loading (13.79 MPa confining pressure). From (Abousleiman et al., 2010).

1.7 Comprehensive Brittleness Model Based on Mechanical and Mineral Properties

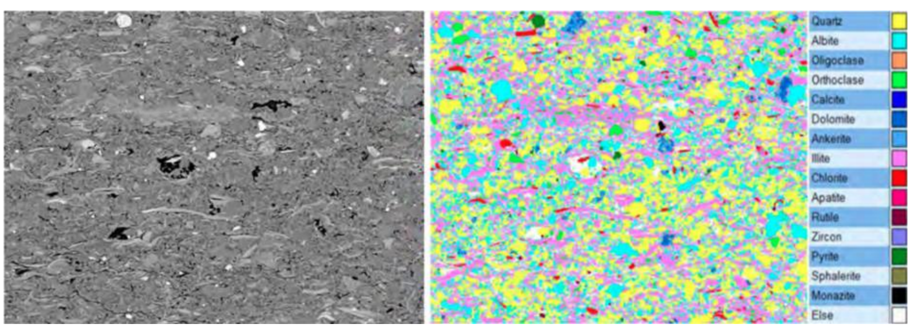

(a)

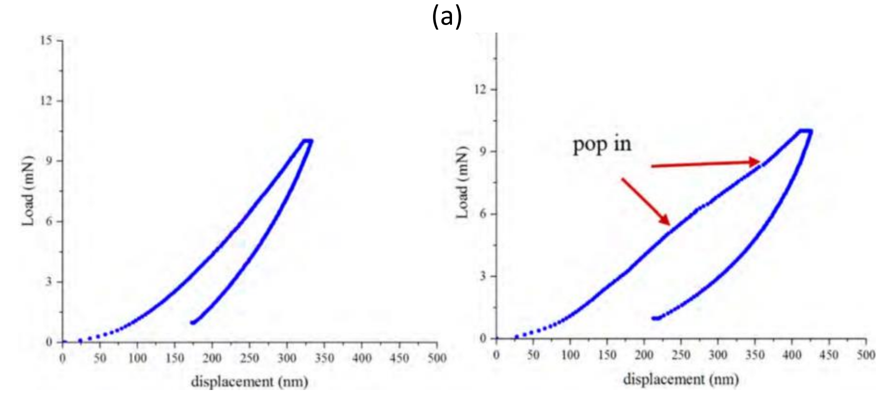

(b)

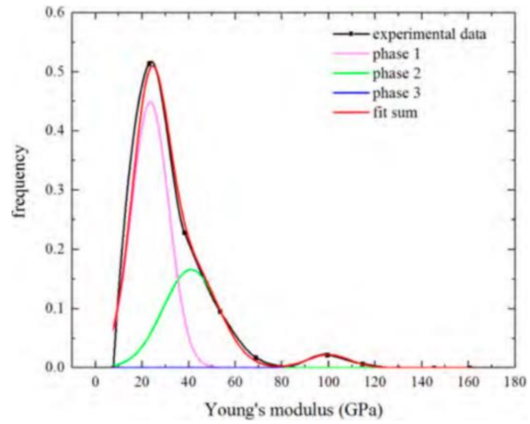

(c)

Figure A- 14: (a) SEM and EDS mapping of the minerals from drill cuttings of shale. (b) Indentation load vs. displacement curves without (left) and with (right) surface heterogeneity of pores/micro-fractures. (c) Deconvolution results for Young's modulus based on indentation measurements. The results for deconvolution analysis should be obtained using identical samples that exclude the samples with heterogeneity ("pop in" displacement). From (Shi et al., 2020).

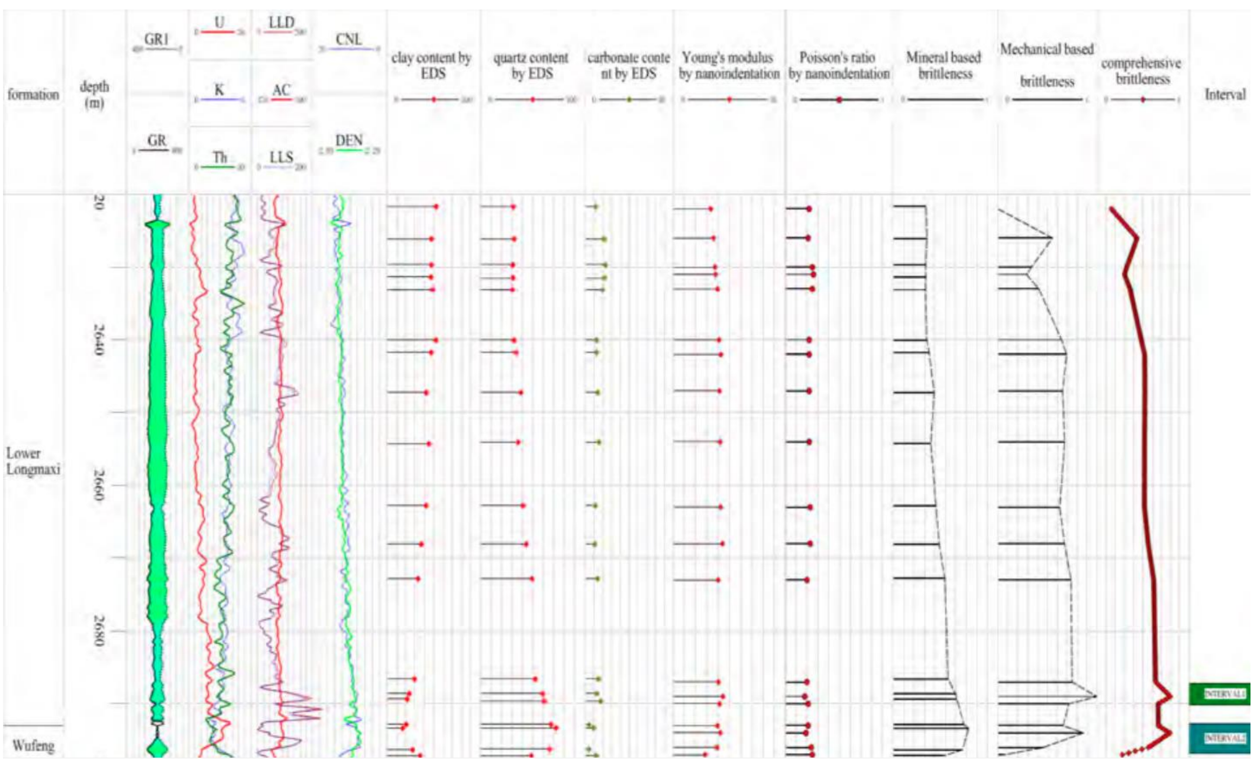

Figure A- 15: Depth vs. comprehensive brittleness (last track) for a shale gas well in Lower Silurian Longmaxi Formation. From (Shi et al., 2020).

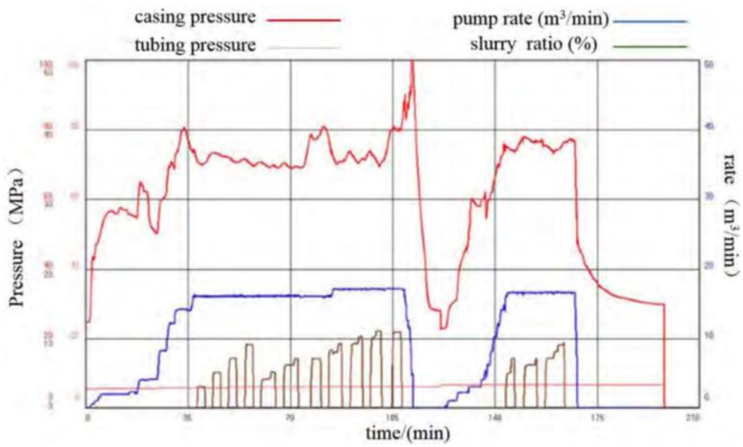

Figure A- 16: HF pressure data for one stage of horizontal shale gas well along interval 1 shown in Figure A- 15.

1.8 Using Drilling Data

1.8.1 Estimating Formation Strength Parameters

Table A- 3: Operating conditions for the drilling tests (Khoshouei and Bagherpour, 2021).

Title	Description
Weight on bit	1000 N
The rotational speed	830 RPM
Drill bit diameter	12 mm
Kind of drill bit	Diamond bit special for hard rocks
Drilling fluid	Water
Acoustic sensor	Acoustic condenser microphone model AR 321
Sound pressure level meter	SPL meter model GM1356
Vibration sensor	ADXL 335
Sampling frequency of the acoustic signal	44,100 kHz
Sampling frequency of the sound level	1 Hz
Sampling frequency of the vibration signal	50 Hz

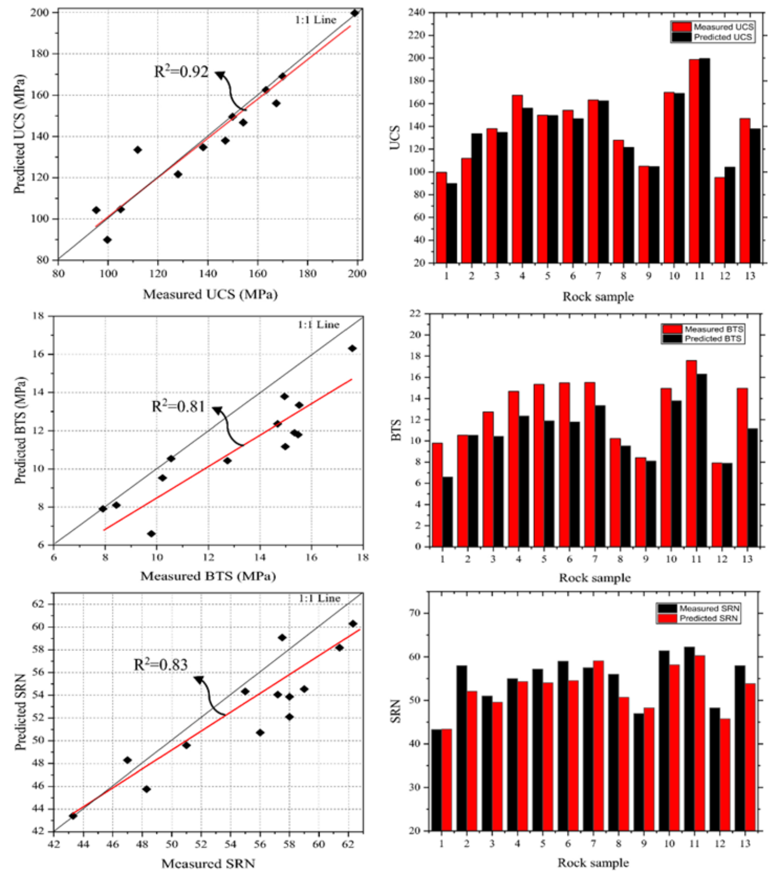

Figure A- 17: The correlation between the measured and predicted mechanical properties of the rock samples. From (Khoshouei and Bagherpour, 2021).

1.8.2 Estimating Dynamic Young's Modulus

Table A- 4: The weights and biases of the optimized ANN model. From (Mahmoud et al., 2021).

Neurons	Training Layer							Output Layer	
	Weights						Biases	Weights	Biases
	WOB, klbf	Torque, kft.lbf	SPP, psi	DSR, rpm	ROP, ft/h	Flowrate, gpm			
1	-4.72	3.23	-2.54	3.57	1.90	3.34	1.07	-1.32	-0.49
2	-11.60	2.07	-1.51	4.81	2.20	0.82	-2.94	0.71	
3	3.61	-3.04	-0.63	-1.13	-0.04	1.27	0.60	1.71	
4	-1.85	-0.41	1.10	4.52	-3.25	-1.52	-0.30	0.85	
5	-0.73	-2.37	1.61	1.83	1.25	-1.32	0.35	-3.59	
6	-1.48	-4.93	-3.09	1.64	0.96	1.56	0.06	1.00	
7	-6.03	0.71	-1.55	3.22	-1.94	-2.68	3.23	-0.87	
8	-0.17	-0.51	-1.10	-5.22	-0.60	2.51	2.74	-1.77	
9	-0.38	0.45	0.71	0.11	2.34	0.32	1.47	3.89	
10	11.92	-28.02	-10.13	-11.00	-10.49	-5.10	9.80	-0.56	
11	-0.69	0.64	0.77	0.18	-0.08	0.90	-0.31	-3.41	
12	-2.50	3.10	0.26	-5.44	-5.12	5.91	3.02	1.38	
13	-6.98	-1.08	-3.58	1.11	-2.57	5.69	0.12	-1.17	
14	1.67	0.03	-2.49	-4.26	-3.33	2.52	1.08	-1.31	
15	-1.39	6.81	-1.24	-9.57	-9.17	1.26	0.23	-0.34	
16	0.76	-1.72	-2.97	0.82	-4.77	-0.33	1.92	-1.09	
17	0.96	0.19	-2.23	-3.12	-3.18	1.89	0.17	1.75	
18	-0.13	2.30	0.82	4.98	-1.23	-1.09	-3.34	-2.11	
19	-15.01	9.79	-0.47	7.63	2.60	1.47	-3.26	0.39	
20	-1.43	1.63	-1.15	4.14	-3.32	-3.22	-1.56	-1.54	
21	-0.77	-2.33	1.49	3.41	-7.87	-0.29	1.09	-0.65	
22	-2.75	0.51	-0.57	3.13	3.18	-3.55	-3.87	1.61	
23	-9.32	3.95	-7.87	3.68	-8.73	3.29	2.77	0.65	
24	-0.57	0.73	0.22	0.54	-2.59	-0.15	-0.73	4.01	
25	1.62	0.75	-1.07	-1.72	-0.34	0.60	-0.34	-3.82	

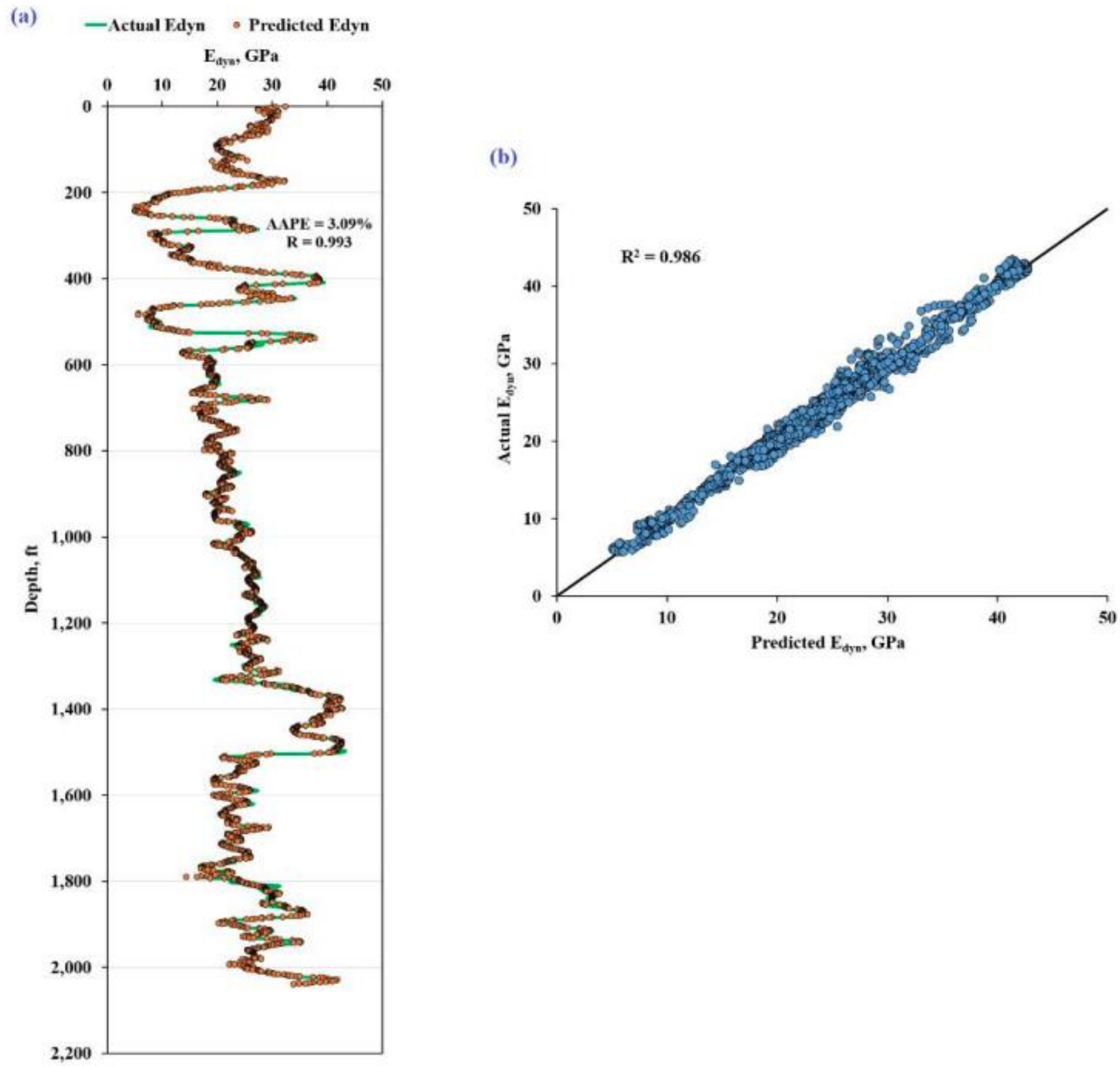

Figure A- 18: Training of the ANN model using 2054 data sample from Well-A. (a) ANN-estimated E_{dyn} and its comparison with the known values of E_{dyn} in Well-A. (b) Cross-plot of the comparison between the ANN-estimated and known values of E_{dyn} in Well-A. From (Mahmoud et al., 2021).

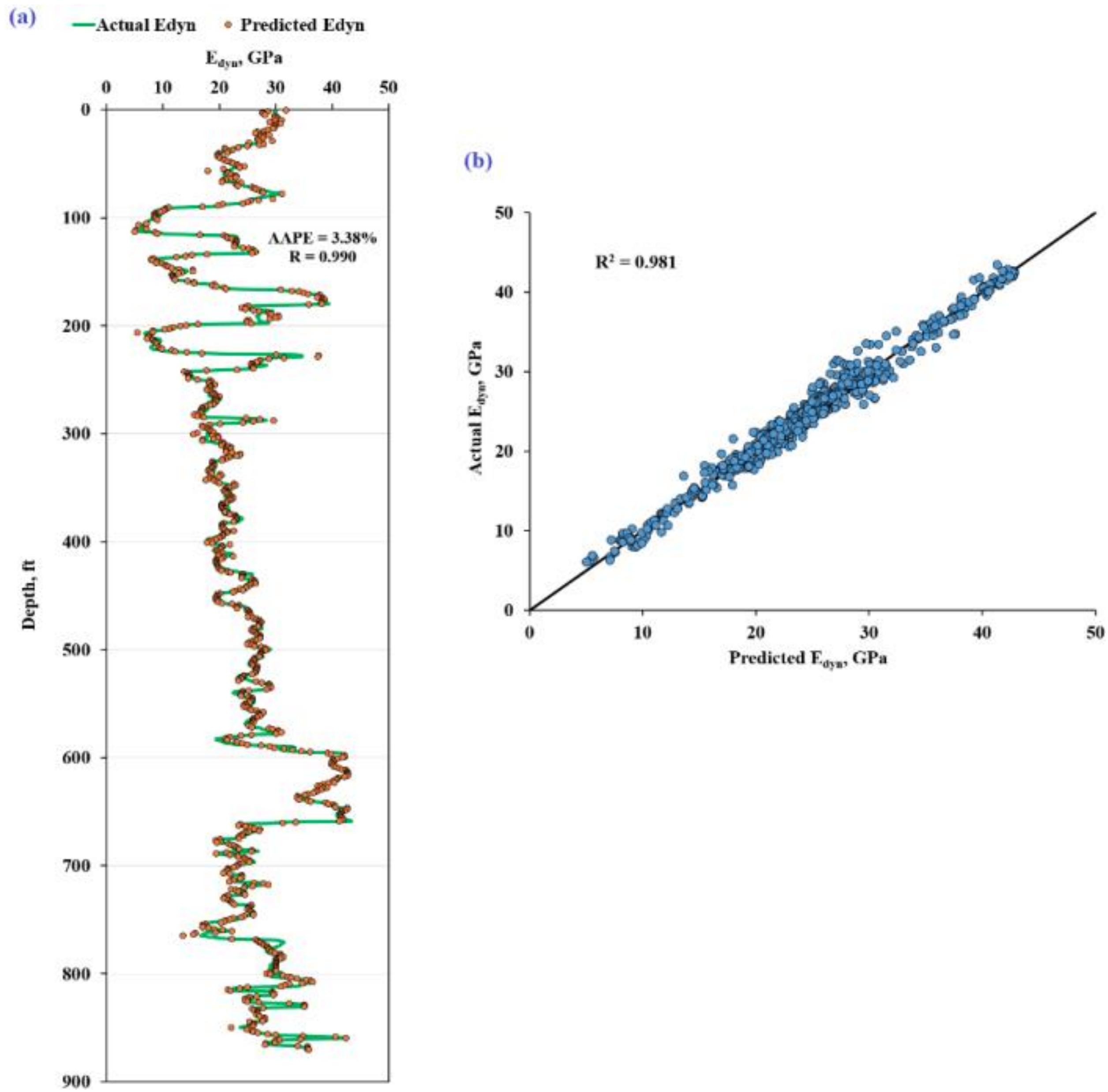

Figure A- 19: Testing of the ANN model using 871 data sample from Well-A. (a) ANN-estimated E_{dyn} and its comparison with the known values of E_{dyn} in Well-B. (b) Cross-plot of the comparison between the ANN-estimated and known values of E_{dyn} in Well-B. From (Mahmoud et al., 2021).

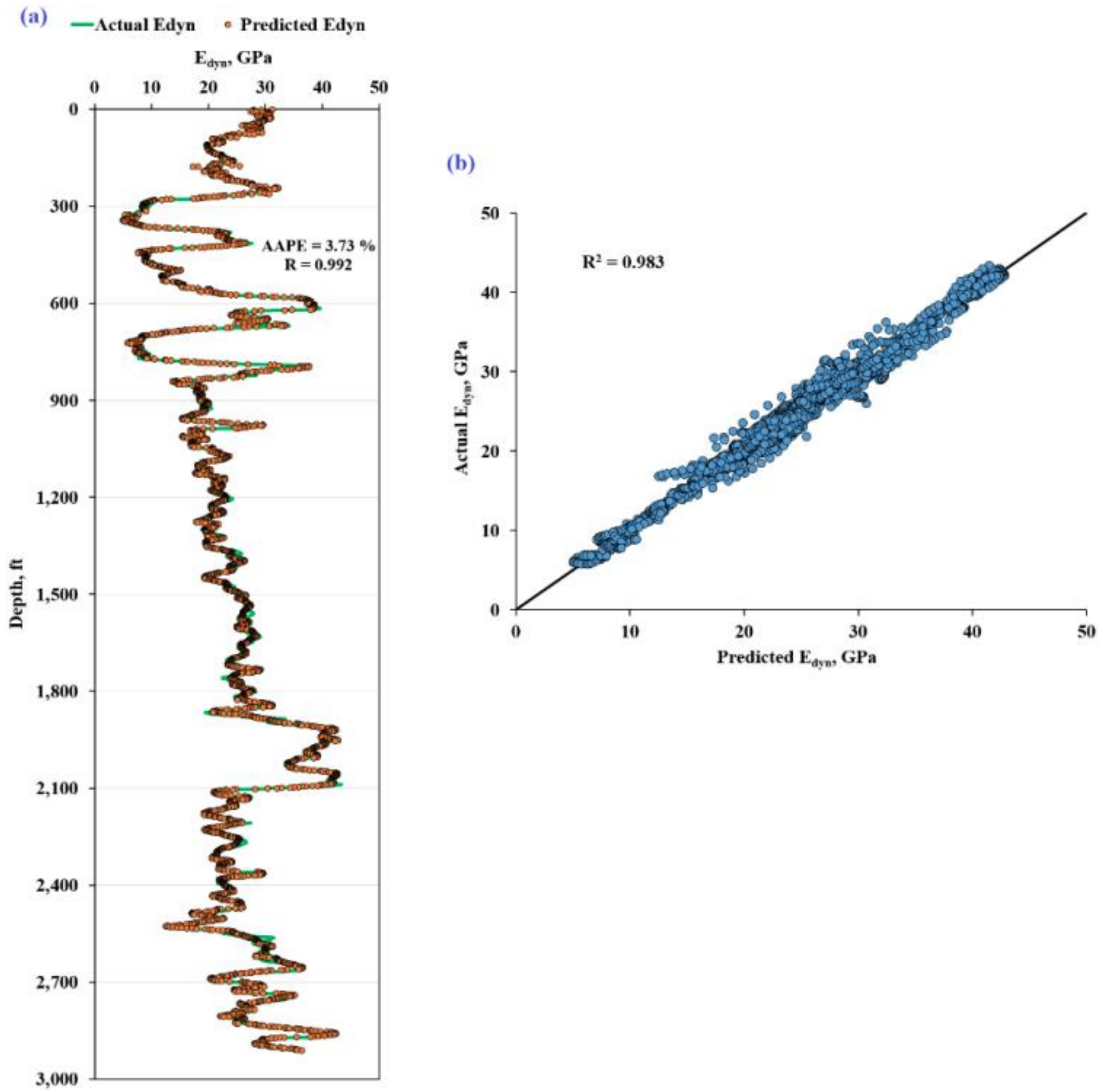

Figure A- 20: Validation of the optimized ANN model using 2912 data samples from Well-C. (a) ANN-estimated E_{dyn} and its comparison with the known values of E_{dyn} in Well-C. (b) Cross-plot of the comparison between the ANN-estimated and known values of E_{dyn} in Well-C. From (Mahmoud et al., 2021).

1.8.3 Estimating Sonic Log

Table A- 5: The weights and biases of the optimized ANN model. From (Hadi and Nygaard, 2021).

Hidden Layer Neurons(i)	Input-Hidden Weight ($w1_i$)					Hidden-Output Weight	Bias	
	TVD	ROP	WOB	RPM	TQ	w_{2_i}	b_{1_i}	b_2
1	-0.00605	0.2387	-0.008	0.0107	0.0807	-14.123	13.772	82.89
2	0.00026	0.2904	0.0261	0.0208	0.0044	-0.672	-6.043	
3	-0.00251	-0.018	-0.097	0.0256	-0.374	6.2408	7.0942	

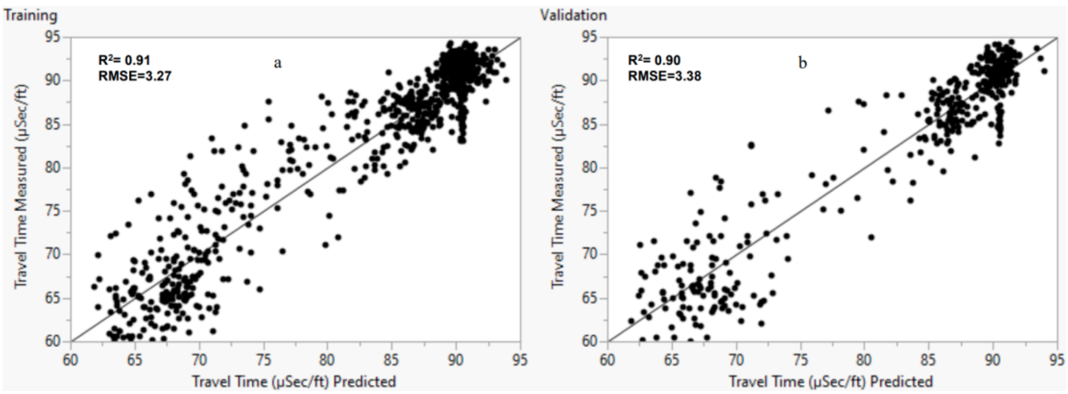

Figure A- 21: Training (R2 of 0.91 and RMSE of 3.27) and validation (R2 of 0.90 and RMSE of 3.2738) of the ANN model for DT and its comparison with the known values of DT. From (Hadi and Nygaard, 2021).

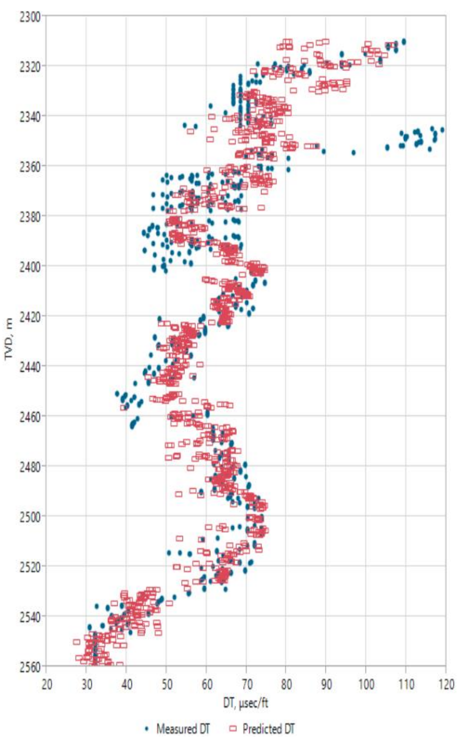

Figure A- 22: Validation of the trained ANN model for DT in another carbonate formation of interest and its comparison with the known values of DT. From (Hadi and Nygaard, 2021).

1.8.4 Identification and Characterization of Fracture Patterns

Time	Duration	Depth	Interpretation	Volume Lost
	s	ft		litre
8:28:00	5405	XX946.8	Open Fracture	-176.62
10:20:00	2405	XX950.37	Open Fracture	-29.99

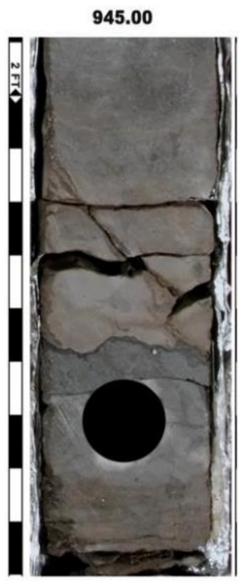

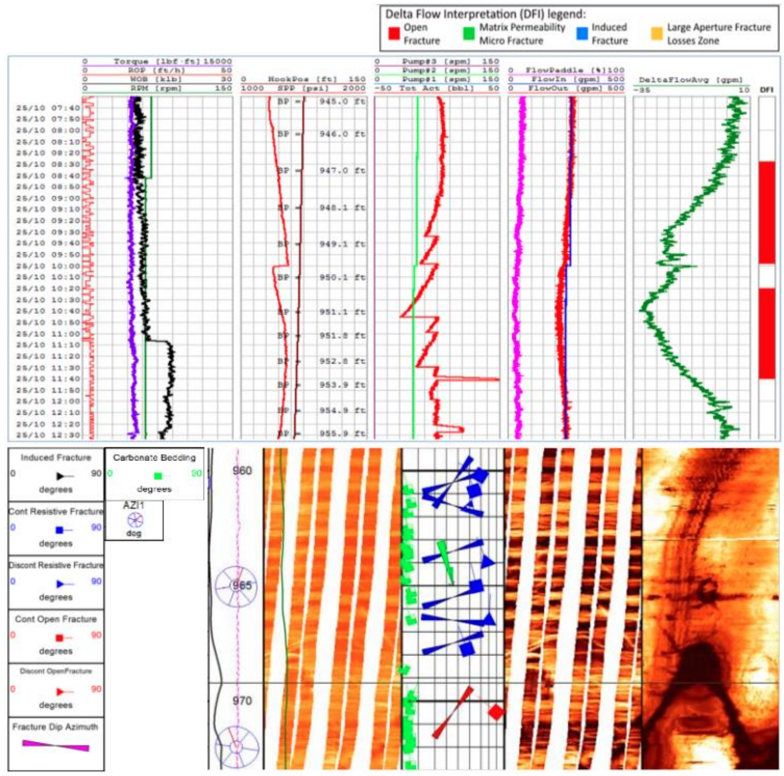

(a)

Time	Duration	Depth	Interpretation	Volume Lost
	s	ft		litre
11:56:00	905	XX990.11	Open Fracture	-3.55
12:15:00	905	XX990.81	Open Fracture	-1.25
12:32:00	905	XX991.4	Open Fracture	-7.92
12:57:00	280	XX992.25	Open Fracture	-0.74

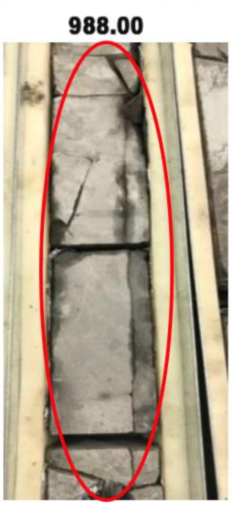

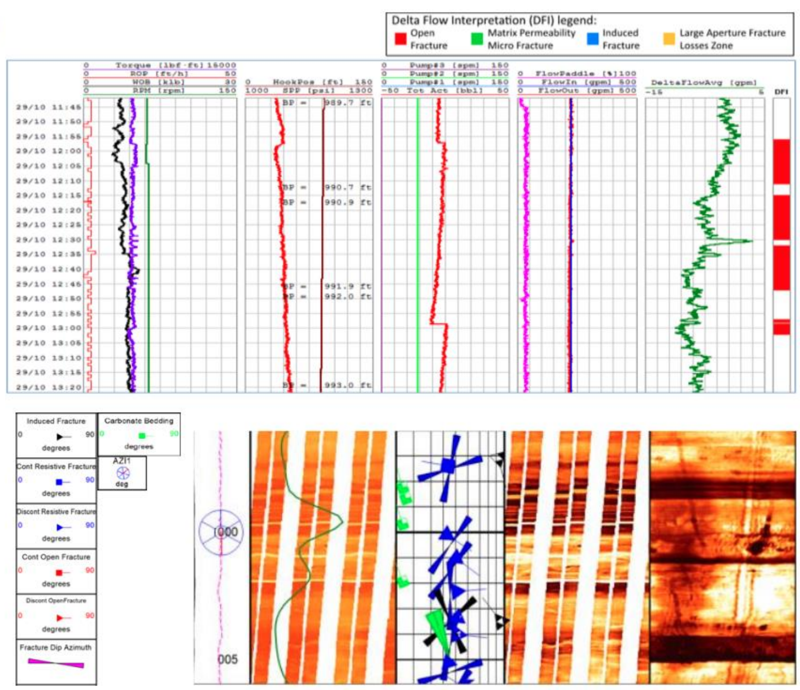

(b)

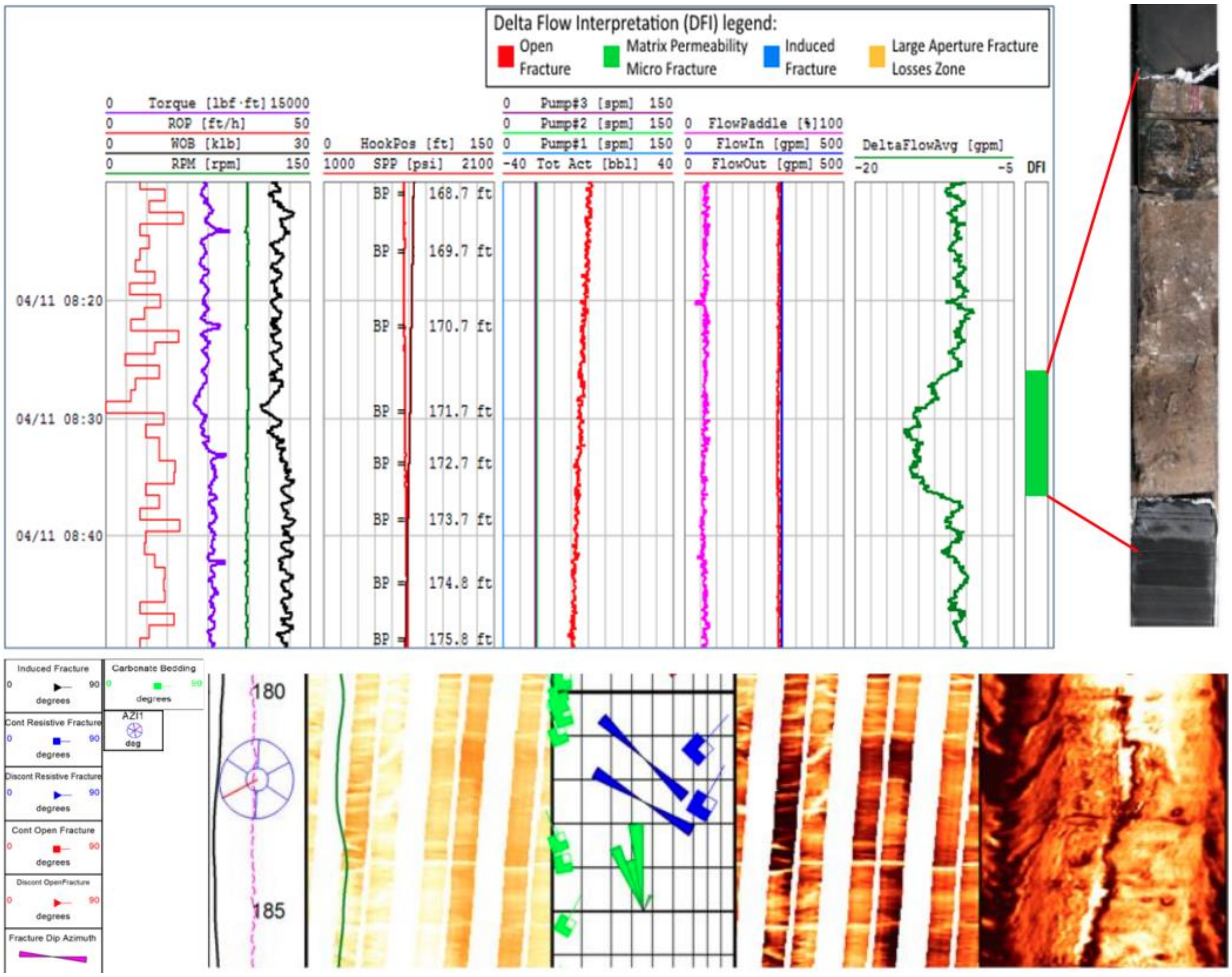

Delta Flow Interpretation (DFI) legend:
Open Fracture
Matrix Permeability Micro Fracture
Induced Fracture
Large Aperture Fracture Losses Zone
0 Torque [lbf·ft] 15000
0 ROP [ft/h] 50
0 WOB [klb] 30
0 RPM [rpm] 150
0 HookPos [ft] 150
1000 SPP [psi] 2100
0 Pump#3 [spm] 150
0 Pump#2 [spm] 150
0 Pump#1 [spm] 150
-40 Tot Act [bbl] 40
0 FlowPaddle [%] 100
0 FlowIn [gpm] 500
0 FlowOut [gpm] 500
DeltaFlowAvg [gpm]
-20 -5
DFI
04/11 08:20
04/11 08:30
04/11 08:40
BP = 168.7 ft
BP = 169.7 ft
BP = 170.7 ft
BP = 171.7 ft
BP = 172.7 ft
BP = 173.7 ft
BP = 174.8 ft
BP = 175.8 ft
Induced Fracture
Carbonate Bedding
Cont Resistive Fracture
Discont Resistive Fracture
Cont Open Fracture
Discont OpenFracture
Fracture Dip Azimuth
AZI1
180
185

(c)

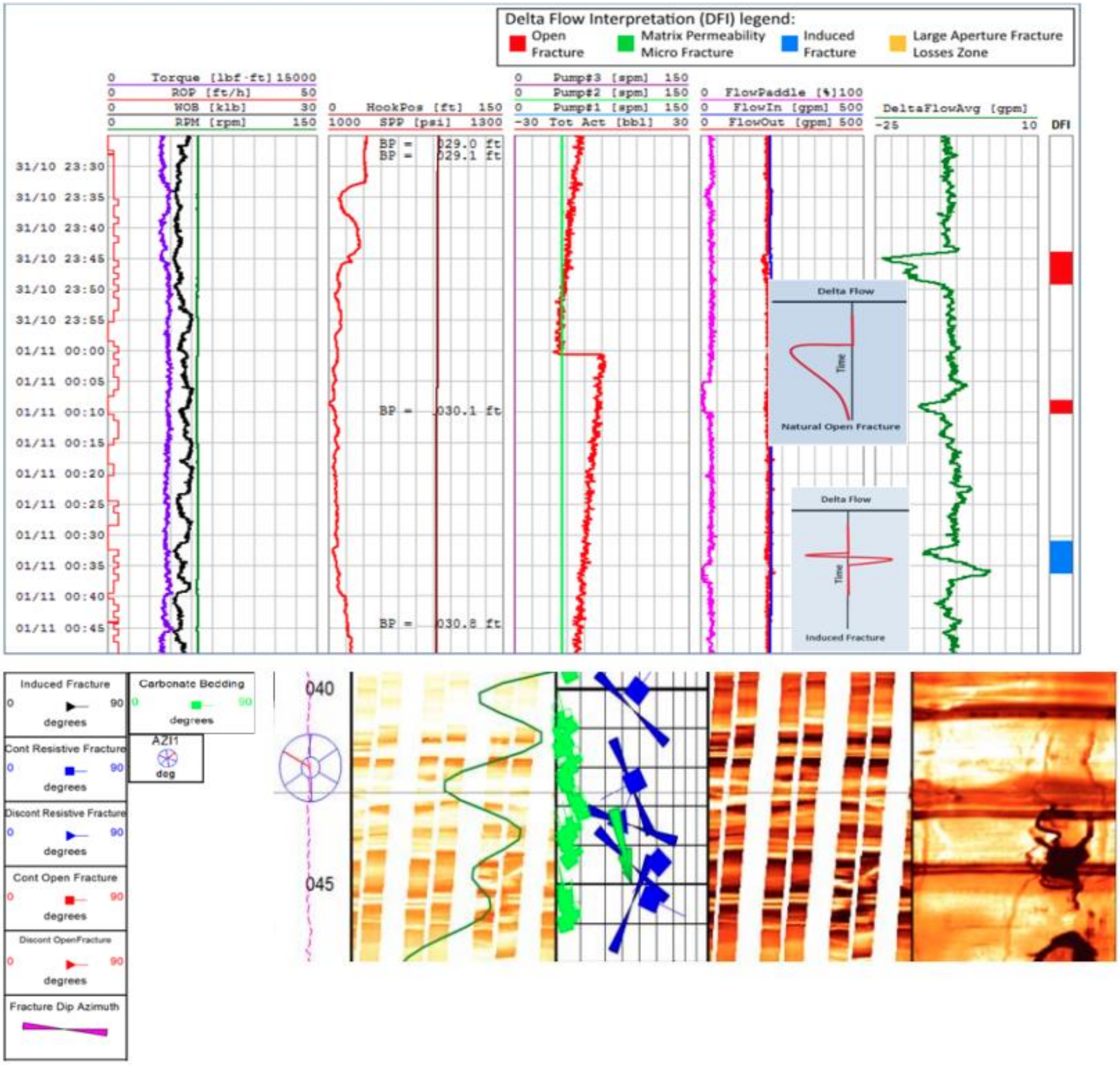

(d)

Figure A- 23: (a) Natural open fractures identified using Delta Flow measurements (top right) and confirmed via core inspection (left), and image log interpretation (bottom right). (b) Natural open fractures identified using Delta Flow measurements (top right) and confirmed via core inspection (left), and image log interpretation (bottom right). (c) Matrix permeability identified using Delta Flow measurements (top) and confirmed via core inspection (top right), but image log interpretation (bottom) cannot detect this type of events. (d) Induced and open open fractures identified using Delta Flow measurements (top) and confirmed via image log interpretation (bottom). From (Dashti et al., 2021).